Turbulent heat transfer in channels with irregular roughness

J. W. R. Peeters[a,b,*], N. D. Sandham[b]

[a]*Energy technology, Delft University of Technology, Leeghwaterstraat 39, 2628 CB Delft, the Netherlands*
[b]*Faculty of Engineering and the Environment, Tizard Building, Highfield, University of Southampton, Southampton SO17 1BJ, United Kingdom*

Abstract

It is well known that rough surfaces affect turbulent flows significantly. How such surfaces affect turbulent heat transfer is less well understood. To gain more insight, we have performed a series of direct numerical simulations of turbulent heat transfer in a channel flow with grit-blasted surfaces. An immersed boundary method is used to account for the rough surface. A source term in the thermal energy balance is used to maximise the analogy between the transport of heat and the transport of streamwise momentum. The wall roughness size is varied from $k^+ = 15$ to k^+=120. Turbulence statistics like mean temperature profile, mean temperature fluctuations and heat fluxes are presented. The stucture of the turbulent temperature field is analysed in detail. Recirculation zones, which are the result of an adverse pressure gradient, have a profound effect on heat transfer. This is important as it leads to the wall-scaled mean temperature profiles being of larger magnitude than the mean velocity profiles both inside and outside the roughness layer. This means that the temperature wall roughness function $\Delta\Theta^+(k_s^+, Pr)$ is different from the momentum wall roughness function $\Delta U^+(k_s^+)$. Since the bulk temperature and velocity depend on $\Delta\Theta^+(k_s^+, Pr)$ and $\Delta U^+(k_s^+)$, it was shown that the Stanton number and the skin friction factor directly depend on $\Delta\Theta^+(k_s^+, Pr)$ and $\Delta U^+(k_s^+)$, respectively. Therefore, the failure of the Reynolds analogy in fully rough conditions can be directly related to the difference between $\Delta\Theta^+(k_s^+, Pr)$ and $\Delta U^+(k_s^+)$.

Keywords: wall roughness, turbulent heat transfer, Direct Numerical Simulation, Reynolds

*Corresponding author
Email address: j.w.r.peeters@tudelft.nl (J. W. R. Peeters)

1. Introduction

Hydrodynamically rough surfaces can be found in many engineering systems. Typical causes of roughness include machining, fouling or corrosion. It is well known that wall roughness affects both the mean flow as well as the turbulent motion of a fluid, which in turn affects skin friction. A well-known result of the effects of roughness is summarised in the form of the Moody-diagram. However, as Flack [11] points out, it is impossible to predict exactly how a rough surface affects the flow in the transitionally rough regime. The effect of roughness on turbulent flows is typically summarised by a single function, which is called the wall roughness function. Recent work from Busse et al. [6] and Thakkar et al. [35] shows that direct numerical simulations of turbulent flows over realistic surfaces can be used to help determine which topological characteristics should be used to predict the wall roughness function. Thakkar et al. [36] have shown that direct numerical simulations of turbulent flow over a grit-blasted surface yields results that are very close to the results that were originally reported by Nikuradse [27].

While the effect of wall roughness on momentum transfer is being extensively investigated, less attention has been given to the effect of wall roughness on turbulent heat transfer. Early research by Martinelli [24], Nunner [28], Dipprey and Sabersky [9] and Yaglom and Kader [39] focussed on finding a relation for the Stanton number in pipes as a function of the skin friction factor, the Reynolds number and the molecular Prandtl number. Their methods combine analytical considerations with experimental results. A theoretical study by Katoh et al. [17] showed that the heat transfer enhancement is typically less than the drag enhancement if the molecular Prandtl number is less than the turbulent Prandtl number. DNS results of turbulent heat transfer in channels with transverse ribs by Nagano et al. [26] showed for $Pr = 0.71$ that heat transfer increases less than drag does and thus, that the Reynolds analogy does not hold. Furthermore, they surmise that the pressure temperature gradient correlation is important in maintaining the turbulent heat flux. Later, Bons [5] evaluated the application of the Reynolds analogy for turbine flows and found that the accuracy of

this analogy decreases dramatically as surface roughness height increases. Both Dipprey and Sabersky [9] and Bons [5] note that increases in the Stanton number are accompanied by even larger increases in the skin friction coefficient. Moreover, Bons [5] explains this phenomenon by reasoning that roughness introduces a pressure drag component to the skin friction coefficient and that there is no corresponding mechanism with respect to the Stanton number. This is logical, since it is known that the existence of mean pressure gradients is the cause of dissimilarity between velocity and temperature fields in perturbed thermal boundary layers, see for instance Kong et al. [21].

Recently, Leonardi et al. [23] and Orlandi et al. [29] used direct numerical simulations to study how regular roughness (such as bars and cubes mounted on the surfaces of a channel) can affect heat transfer. These studies focused on heat transfer modification through passive means. However, they did not show how irregular rough surfaces, such as surfaces affected by machining or corrosion, affect heat transfer. Forooghi et al. [13] showed DNS results of momentum and heat transfer in a channel with combustion deposits. They too found that the Reynolds analogy is less accurate with increasing wall roughness height. Forooghi et al. [12] subsequently investigated systematically the effect of effective surface slope, roughness density and roughness height on heat transfer. They note that an effect known as sheltering leads to a decrease in the Stanton number for high roughness densities and that different roughness shapes affect heat and momentum transfer differently. Furthermore, they presented a reasonable correlation between the Reynolds analogy factor and sand grain equivalent roughness height, k_s^+. Another model for the Reynolds analogy was recently derived by Aupoix [4], which is dependent on both the momentum and scalar wall roughness functions and a novel turbulent Prandtl number relation. It was shown that this new model yields enhanced heat transfer predictions.

The goal of the present study is to gain insight into the modification of turbulent heat transfer by an irregular rough surface, which has been shown to act as a surrogate for Nikuradse-type roughness. In particular, we will present a detailed analysis of the effect of wall roughness on turbulent heat transfer statistics, structural effects and the parametrisation

of these effects, such as the temperature wall roughness function $\Delta\Theta^+$ and various Stanton number relations.

2. Methodology

2.1. Numerical methods

To understand how wall roughness affects heat transfer, a numerical approach is used to solve the dimensionless incompressible Navier-Stokes equations and the transport equation for the temperature θ with uniform heat generation Q:

$$\boldsymbol{\nabla} \cdot \boldsymbol{u} = 0 \tag{1}$$

$$\partial_t \boldsymbol{u} + \boldsymbol{u} \cdot \boldsymbol{\nabla} \boldsymbol{u} = -\boldsymbol{\nabla} p + Re_\tau^{-1} \boldsymbol{\nabla}^2 \boldsymbol{u} \tag{2}$$

$$\partial_t \theta + \boldsymbol{u} \cdot \boldsymbol{\nabla} \theta = Pe_\tau^{-1} \boldsymbol{\nabla}^2 \theta + Q, \tag{3}$$

where $\boldsymbol{u}$ is the velocity vector, $Re_\tau \equiv u_\tau \delta / \nu$ the Reynolds number (based on the friction velocity u_τ), $Pe_\tau \equiv Re_\tau Pr$, the Peclet number (with Pr being the molecular Prandtl number) and $\boldsymbol{\nabla} p = \boldsymbol{\nabla} p_{hy} + \Pi$. p_{hy} is the hydrodynamic pressure while Π is the driving force and Q is the internal heat generation. The velocity vector and the temperature are scaled by $u_\tau \equiv \sqrt{-(\delta/\rho)\Pi}$ and $T_\tau \equiv q_w/(\rho c_p u_\tau)$, which results in Π and Q being equal to unity for a channel with a mean half-height δ. This approach is similar to the studies by Busse et al. 2015 and Zhou et al. 2017.

A simple channel geometry with roughness on both isothermal walls is considered. The domain size ($L_x \times L_y \times L_z$) is $5.63\delta \times 2\delta \times 2.815\delta$ in the streamwise, wall normal and spanwise directions. Periodic boundary conditions are used in the streamwise and spanwise directions. To account for the wall roughness, the immersed boundary method of Fadlun et al. [10] is used. At the first grid point outside the immersed boundary, a velocity is enforced that is based on the interpolation by a quadratic polynomial.

Figure 2 shows height maps of three different rough surfaces that are considered in this study. The first (figure 2a) is a filtered surface scan of a grit-blasted surface (see also Busse et al. [6] and Busse et al. [7]). The second (figure 2b) and third surface (figure 2c) are tiled versions of the first and are shrunk by a factor of two and four, respectively. The method of

tiling was previously described by Thakkar et al. [36]. These surfaces have been shown to act as a surrogate for Nikuradse-type roughness. Figure 2 shows a schematic of a rough surface in a channel. The surface height s is measured from the lowest point of the computational domain to the surface. The mean surface height is located at $y/\delta = 0$.

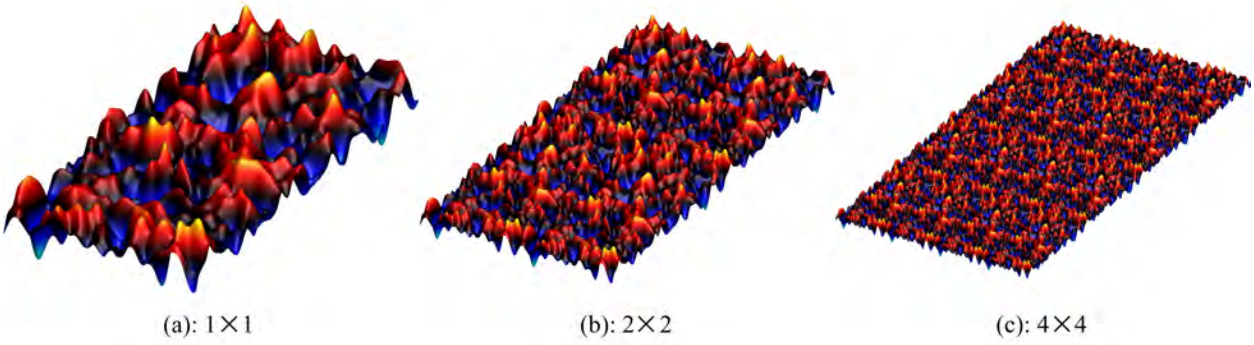

Figure 1: Height maps of three different rough walls. (a) The filtered result of a grit-blasted surface. (b) a 2×2 tiled version of the first surface. (c) a 4×4 tiled version of the first surface.

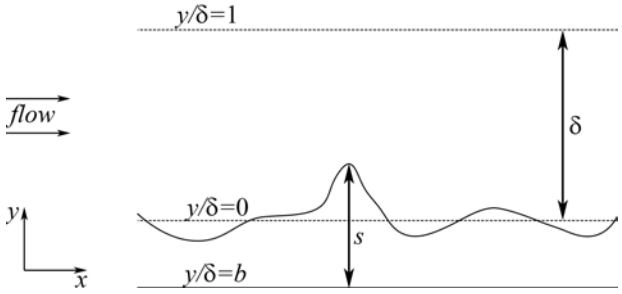

Figure 2: Schematic of half the computational domain. δ is the mean channel half height measured from the surface to the centreline of the channel. s is the surface height measured from the lowest point of the computational domain to the surface. b is the lowest point in the domain and equals -0.16 (1×1 surface), -0.08 (2×2 surface) and -0.04 (4×4 surface).

2.2. Direct numerical simulations

Multiple new cases with irregular roughness are considered. The details of these cases are presented in table 1. The roughness height is varied from $k^+ = 15$ to $k^+ = 120$, or $k_s^+ = 13$ to $k_s^+ = 102$, as $k_s^+ \approx 0.87k^+$, with k^+ being the mean peak-to-valley-height. To calculate this quantity, the surface is first partitioned into 5×5 tiles. The mean peak to valley height is then calculated as the average of the maximum peak-to-valley-heights of the different tiles,

Table 1: Details of the DNS cases. N denotes the number of gridpoints, while x, y, z denote the streamwise, wall-normal and spanwise directions, respectively.

k^+	k/δ	Re_τ	Re_b	N $(x \times y \times z)$	surface
0	0	180	5.7×10^3	$196 \times 196 \times 140$	smooth
0	0	360	12.6×10^3	$336 \times 196 \times 280$	smooth
0	0	540	20.0×10^3	$576 \times 432 \times 288$	smooth
0	0	720	27.8×10^3	$912 \times 576 \times 480$	smooth
15	1/12	180	4.6×10^3	$560 \times 224 \times 280$	2×2 (figure 1b)
30	1/6	180	3.5×10^3	$280 \times 280 \times 140$	1×1 (figure 1a)
15	1/24	360	11.1×10^3	$1152 \times 384 \times 576$	4×4 (figure 1c)
30	1/12	360	9.5×10^3	$560 \times 392 \times 280$	2×2 (figure 1b)
60	1/6	360	7.9×10^3	$560 \times 420 \times 280$	1×1 (figure 1a)
90	1/6	540	11.8×10^3	$624 \times 816 \times 312$	1×1 (figure 1a)
120	1/6	720	15.5×10^3	$816 \times 1008 \times 432$	1×1 (figure 1a)

see Thakkar et al. [35]. Different Reynolds numbers ($Re_\tau \equiv u_\tau \delta/\nu$) are considered, varying from $Re_\tau = 180$ to $Re_\tau = 720$. The molecular Prandtl number Pr is assumed to be equal to unity. Furthermore, the rough walls are kept cool, $\theta_w = 0$, while the bulk of the fluid is volumetrically heated.

2.3. Domain size and validation

It is vital that the domain size is large enough to capture all scales of motion. Results by Coceal et al. [8] demonstrated that turbulence statistics of flows over rough walls can be captured accurately while using relatively small domain sizes. The focus of this study is to invesitgate how wall roughness affects heat transfer. Therefore, stream- and spanwise autocorrelations of the temperature fluctuations $R_{\theta'\theta'}$ were calculated first; these are shown in figure 3. These results inidicate that the domain is large enough to capture the largest thermal structures.

The aforementioned numerical methods were validated by simulating different cases that were previously described by Busse et al. [7], Thakkar et al. [36] and Kim et al. [20]. The Reynolds number for these cases is equal to 180. The details of the validation cases are listed in table 1. Figure 4a shows that there is excellent agreement between the previous and

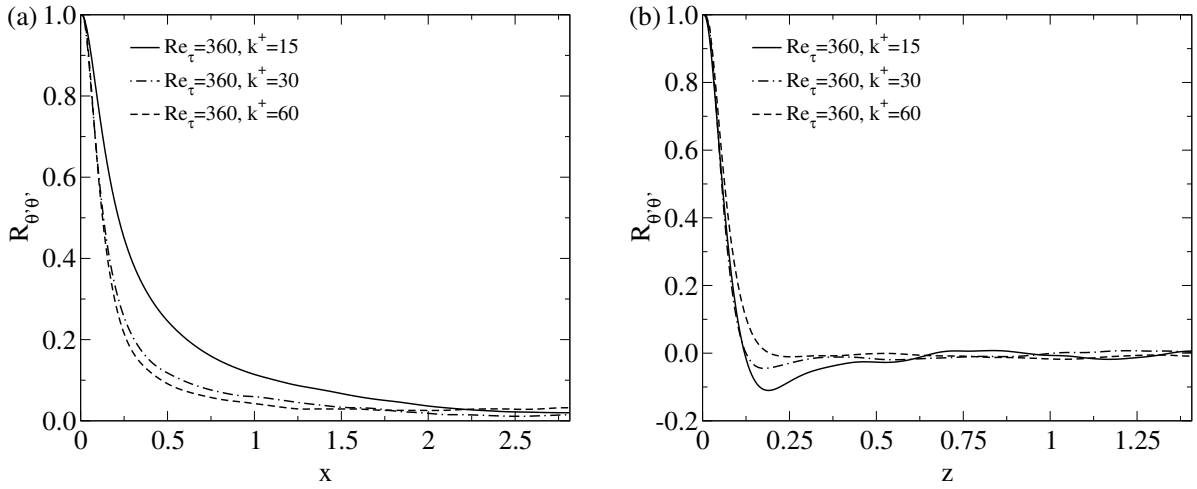

Figure 3: a) Autocorrelation function $R_{\theta'\theta'}$ at $y^+ = 15$ as a function of the streamwise coordinate x. b) Autocorrelation function $R_{\theta'\theta'}$ at $y^+ = 15$ as a function of the spanwise coordinate z.

present results with regards to the mean velocity profiles. As a result, there is also very good agreement in terms of the wall roughness function ΔU^+. Figure 4b shows the comparison between mean scalar profiles that were obtained by Kim and Moin [19] and the present code. There is again excellent agreement between the current code and the literature results.

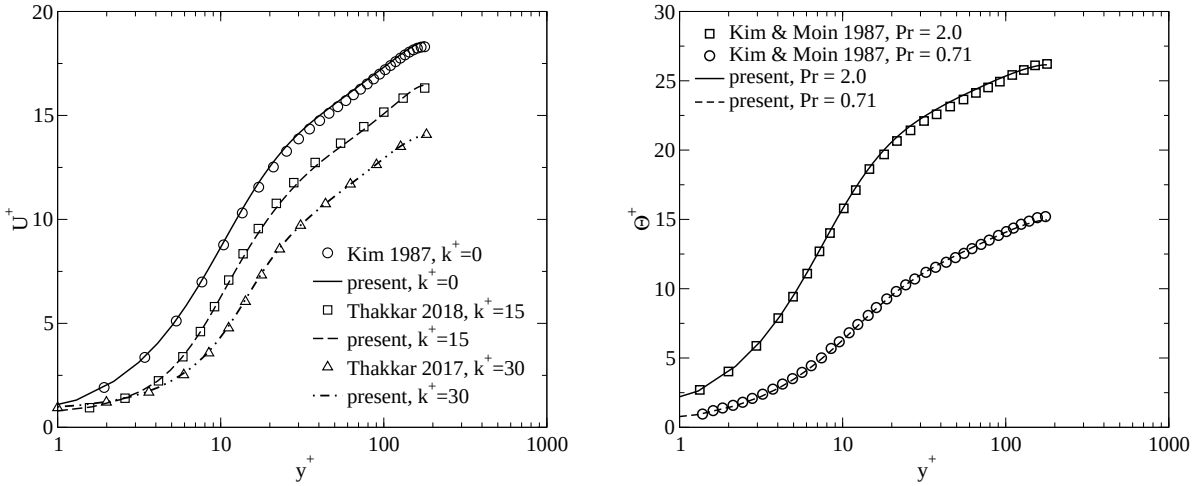

Figure 4: Comparison of mean velocity and temperature profiles for $k^+ = 0, 15$ and 30 at $Re_\tau = 180$ with results from Busse et al. [7], Thakkar et al. [36], Kim et al. [20] and Kim and Moin [19].

3. Mean statistics

From the DNS various temperature statistics are obtained. We will first discuss the mean temperature profiles of the different cases. Subsequently, we will investigate how turbulent thermal fluctuations as well as the turbulent heat flux are affected.

3.1. Averaging procedure

Before discussing the mean statistics, we will first detail the averaging procedure that is employed. The mean temperature is obtained by plane averaging the time averaged temperature $\overline{\theta}$ over the area that is occupied by the fluid:

$$\Theta = \langle \overline{\theta} \rangle = \frac{1}{S} \int_S \psi \overline{\theta} dS, \tag{4}$$

where ψ is an indicator function that is equal to unity inside and zero outside the fluid, and where $\overline{(...)}$ denotes the time averaged temperature and S denotes a plane parallel to the wall. Similarly, U is obtained by plane averaging the time averaged streamwise velocity $\overline{u}$. Instantaneous fluctuations of the temperature are defined as $\theta' = \theta - \overline{\theta}$. Similarly, $u' = u - \overline{u}$ and $v' = v - \overline{v}$ for the streamwise and wall normal velocities, respectively. These fluctuations give rise to the Reynolds stresses and heat fluxes. Unless noted otherwise, the mean statistics will be presented as plane- and time-averaged quantities.

3.2. Mean temperature profile

Figure 5 shows the mean temperature profiles $\Theta(y^+)$ for the cases for which $Re_\tau = 360$ (a) and $k/\delta = 1/6$ (b). The mean temperature profiles show an increasing downward shift with increasing wall roughness height for the region $y^+ \gtrapprox 10$, while showing an upward shift for $y^+ \lessapprox 1$, which means that there is increased heat transfer towards $y/\delta = 0$. This is qualitatively similar to the velocity profiles that were shown by Busse et al. [7]. However, the magnitude of the downward shift is larger for the velocity profiles than it it is for the temperature profiles; this difference will be discussed later in section 5.1.

From figure 6(a) it can be seen that the temperature defect profile, i.e. $\Theta_c - \Theta(y/\delta)$ (with Θ_c being the mean centreline temperature) shows a good collapse for $y/\delta \gtrapprox 0.06$; this value means that the collapse of the temperature defect profile starts much closer to the centre of

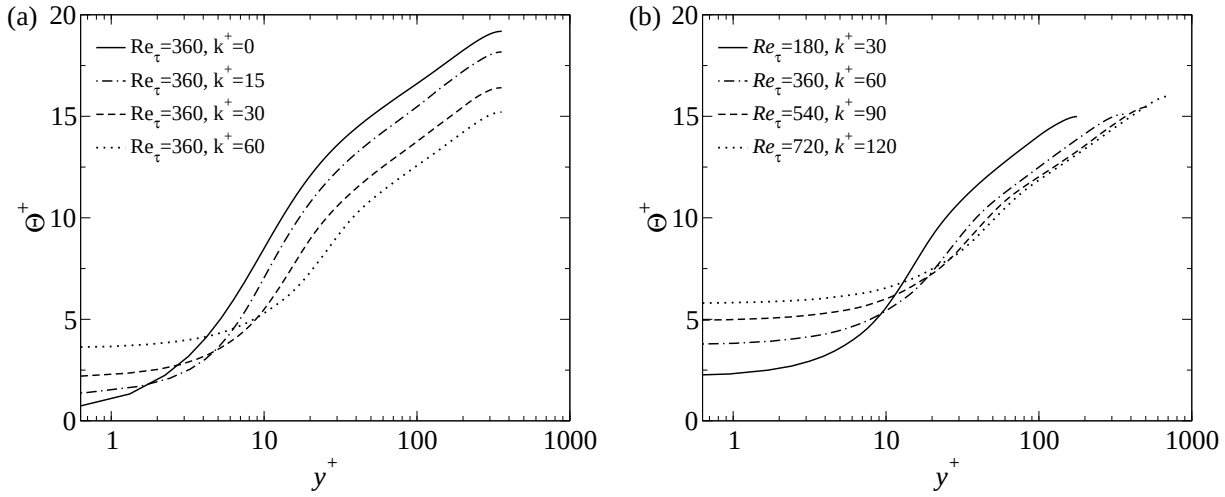

Figure 5: a) mean temperature profiles for $Re_\tau = 360$. b) mean temperature profiles for $k/\delta = 1/6$.

the roughness layer ($y/\delta = 0$) than the collapse of the velocity defect profile, which shows a collapse for $y/\delta \gtrapprox 0.20$ (which was shown in Thakkar et al. [36]).

By applying similarity arguments between momentum transfer and heat transfer, a log-law can be found for the mean temperature profile; see Landau and Lifshitz [22] or Kader and Yaglom [16]. According to Kader [15] the log-region of the mean temperature profile Θ (in the absence of wall roughness) can be described as,

$$\Theta^+(y^+) = \frac{Pr_t}{\kappa}\ln(y^+) + \beta(Pr), \tag{5}$$

where $\beta(Pr) = (3.85Pr^{1/3} - 1.3)^2 + (Pr_t/\kappa)\ln(Pr)$, Pr_t is the turbulent Prandtl number and κ the von Karman constant. In addition, a temperature diagnostic function can be defined as $\gamma_\Theta \equiv y^+ d\Theta^+/dy^+$. Analogous to the diagnostic function for momentum, γ_Θ can be used to determine the factor Pr_t/κ. Figure 6(b) shows a reasonably flat profile of the temperature diagnostic function in the region $\psi < y/\delta < 0.6$, where $\psi \equiv \max(50/Re_\tau, k/\delta)$. From equation (5), it follows that $\gamma_\Theta = Pr_t/\kappa$. After assuming that $\kappa = 0.4$, Pr_t can be determined, see table 2. The values of Pr_t reported here fall within the range $Pr_t = 0.85 - 1$ that is typically assumed in literature. The computed values are slightly higher than the values used by Abe and Antonia [1] (who use $Pr_t/\kappa = 1/0.46$, and $\kappa = 0.39$ which means that $Pr_t \approx 0.85$), or Kader and Yaglom [16] ($Pr_t = 0.85$) or Landau and Lifshitz

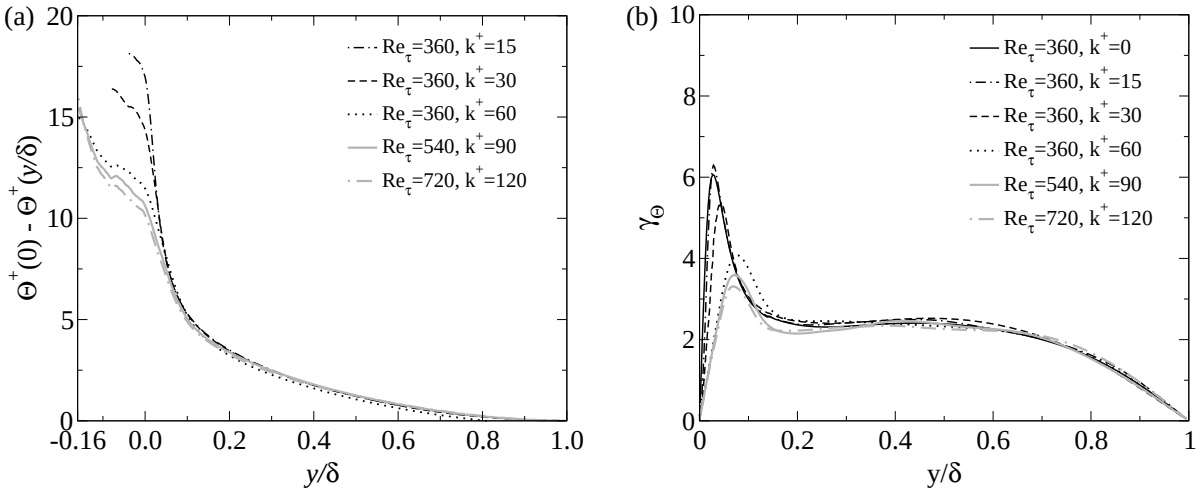

Figure 6: a) temperature defect profiles. b) Temperature diagnostic function.

Table 2: The turbulent Prandtl number Pr_t for cases with different roughness sizes. It is assumed that $\kappa = 0.4$.

Re_τ=360, k^+=15	Re_τ = 360, k^+=30	Re_τ = 360, k^+=60	Re_τ = 540, k^+=90	Re_τ=720, k^+ = 120
0.95	0.96	0.98	0.91	0.91

[22] ($Pr_t = 0.9$). The slightly higher results could be due to the diagnostic approach, the low Reynolds number of the simulations, or due to roughness. Spalart and Strelets [34] proposed a method to determine an effective Prandtl number inside a recirculation bubble as Pr_{eff} . $Pr_{eff} = \nu_{eff}/\alpha_{eff}$, where: $\nu_{eff} = -\langle\overline{u_i'u_j'}\rangle \langle\overline{S_{ij}}\rangle/(2\langle\overline{S_{ij}}\rangle \langle\overline{S_{ij}}\rangle)$ and $\alpha_{eff} = -\langle\overline{u_i'\theta'}\rangle\langle\partial\overline{\theta}/\partial x_i\rangle/(\langle\partial\overline{\theta}/\partial x_i\rangle)^2$. Far away from the wall, $Pr_{eff} \approx Pr_t$. Profiles of Pr_{eff} are shown in figure 7. Pr_{eff} is very similar in the $k^+ = 0$ and the $k^+ = 15$ cases. However, for larger k^+, Pr_{eff} shows a peak value just below the plane $y/\delta = 0$. The peak value is more obvious in the $k/\delta = 1/6$ cases. This peak indicates that the effective thermal diffusivity is much smaller here. Therefore, the region $y/\delta < 0$ can be said to act as a thermal resistance. Meinders et al. [25] showed that a recirculation zone behind a single wall mounted cube acts as a thermal resistance. This is further investigated in section 4.3. Further away from the wall, Pr_{eff} decreases with wall distance; a feature that is intrinsically linked to the unmixedness of the scalar, see Guezennec et al. [14], Abe and Antonia [1, 2]. Furthermore,

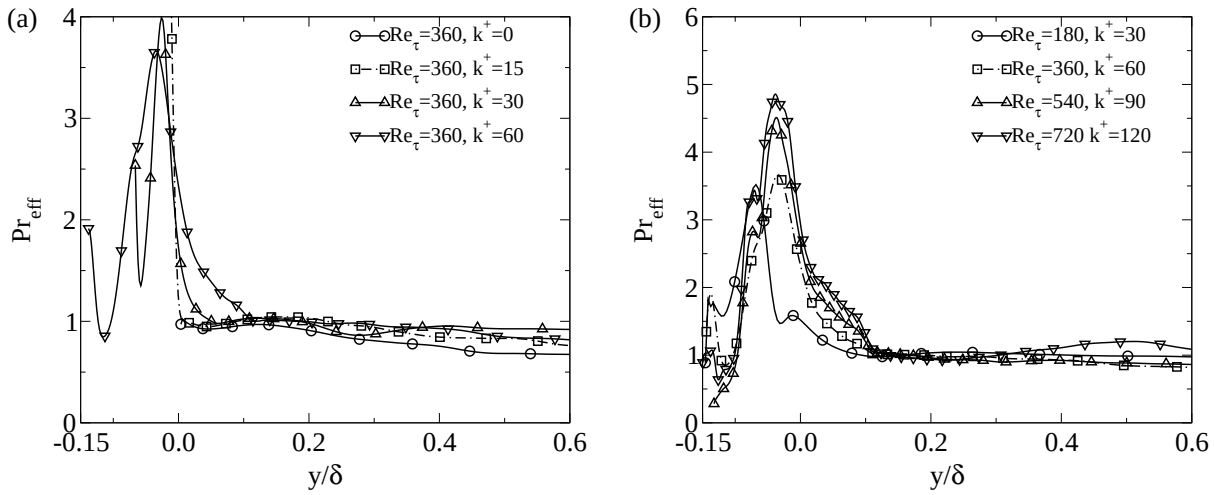

Figure 7: a) mean temperature profiles for $Re_\tau = 360$. b) mean temperature profiles for $k/\delta = 1/6$.

far away from the wall, Pr_{eff} is larger in the simulations with roughness, than Pr_t in the smooth channel case. These results indicate that roughness does indeed affect Pr_t.

3.3. Turbulent thermal fluctuations

As was mentioned before, the thermal fluctuations due to the turbulent motion of the fluid are defined as $\theta' = \theta - \overline{\theta}$. Figure 8 shows the mean square values of the thermal fluctuations $\langle\overline{(\theta')^2}\rangle$ for the different simulated cases.

For the $Re_\tau = 360$ cases, the location of the peak of the fluctuations, $y_{(\theta')^2,max}$, moves further away from the rough surface, as k^+ increases. The different $(\theta')^2$ ($k^+ \neq 0$) profiles collapse well with $(\theta')^2$ ($k^+ = 0$) in the region where $y^+ > k^+$. All profiles simultaneously collapse for approximately $y^+ > 100$. The shift in $y_{(\theta')^2,max}$ is also visible in the cases where $k/\delta = 1/6$. In all cases (except the $Re_\tau = 360, k^+ = 15$ case), $y_{(\theta')^2,max} < k^+$. Furthermore, as k^+ increases, the ratio $y_{(\theta')^2,max}/k^+$ decreases, which means that $y_{(\theta')^2,max}$ lies 'deeper' inside the roughness canopy as k^+ increases. However, for $k/\delta = 1/6$, the variance does not fully collapse in the outer region of the flow, indicating a minor Reynolds number dependence.

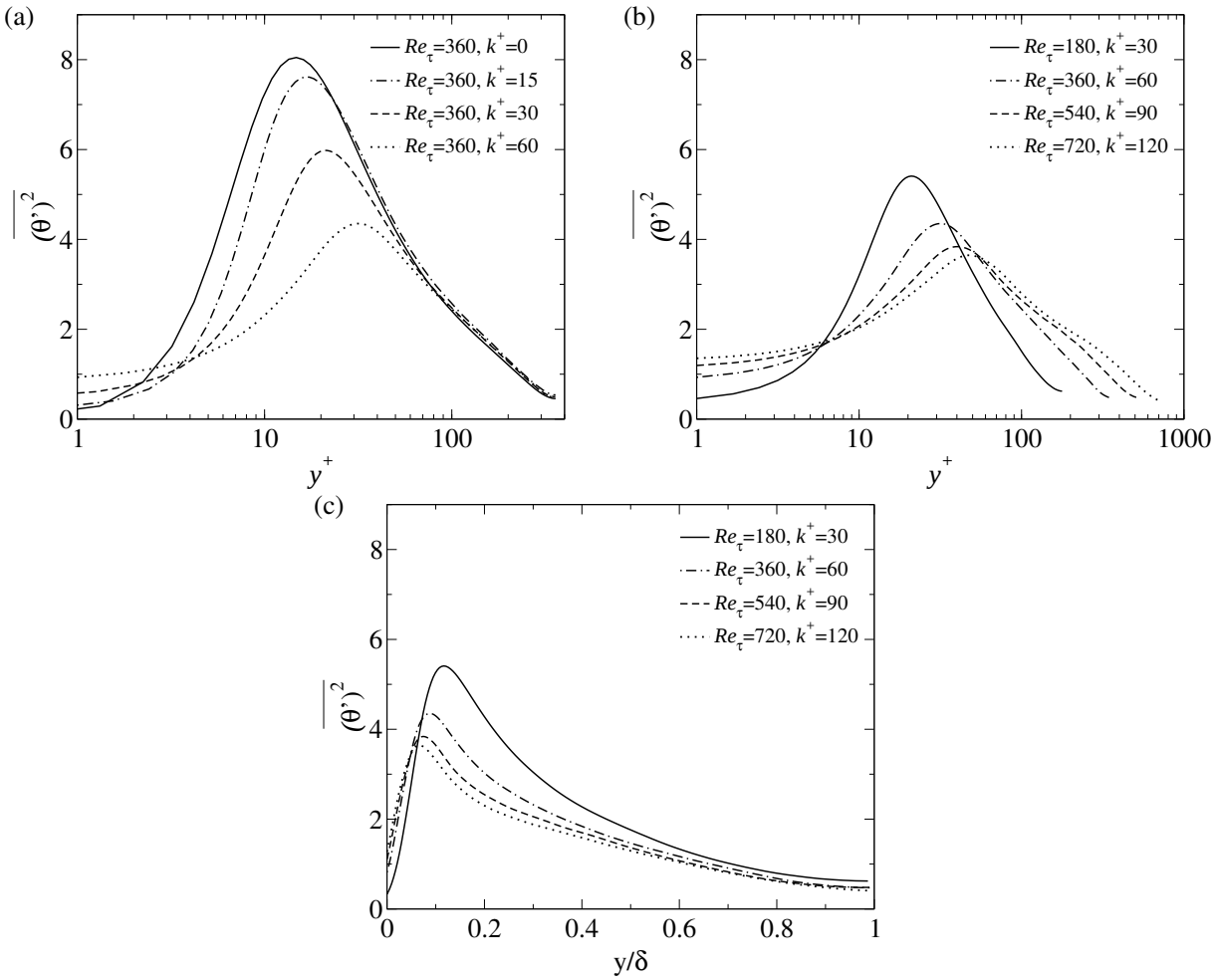

Figure 8: a) $\overline{(\theta')^2}$ normalized by T_τ^2 for $Re_\tau = 360$. b) $\overline{(\theta')^2}$ for $k/\delta = 1/6$. c) Same as b), except that $\overline{(\theta')^2}$ is plotted against y/δ .

3.4. Reynolds stresses and heat fluxes

The temperature fluctuations θ' and velocity fluctuations u' and v' give rise to significant mean Reynolds stresses and heat fluxes. In figure 9, we compare $\overline{v'\theta'}$ with $\overline{v'u'}$ and $\overline{u'\theta'}$ with $\overline{u'u'}$ for the range $k^+ = 0 - 120$. In all cases, $\overline{v'\theta'}$ is practically identical to $\overline{v'u'}$. This is not the case for $\overline{u'\theta'}$ and $\overline{u'u'}$. At small k^+, $\overline{u'\theta'}$ and $\overline{u'u'}$ are very similar up to $y^+ \approx 30$. However, at large wall roughness sizes, $\overline{u'\theta'}$ is smaller than $\overline{u'u'}$. This difference between the streamwise heat flux and $\overline{u'u'}$ grows as k^+ increases. At $k^+ = 30$, the difference is clearly visible for $y^+ > 15$, but for larger k^+, this difference extends to well below $y^+ = 10$. The magnitude of both $\overline{u'u'}$ and $\overline{u'\theta'}$ increase near $y^+ = 1$ for increasing k^+. The increasing

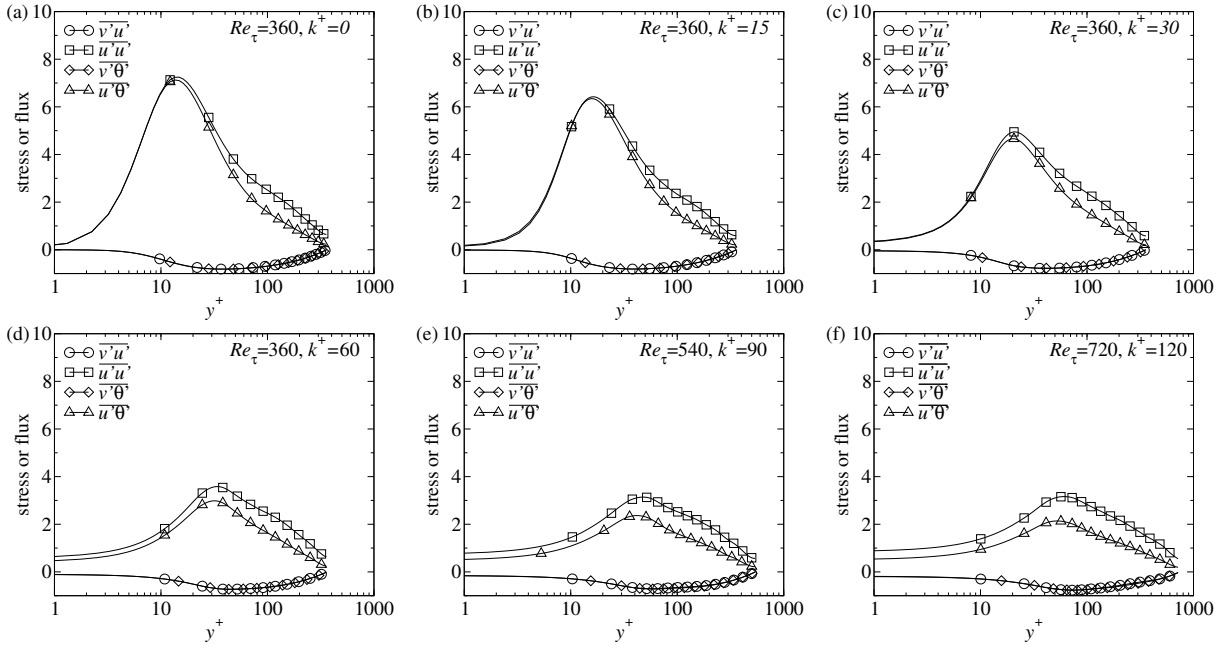

Figure 9: The wall normal Reynolds stress ($\overline{v'u'}$, normalized by u_τ^2) and heat flux ($\overline{v'\theta'}$, normalized by $u_\tau T_\tau$) for cases with different k^+. In the top row (a/b/c), $Re_\tau = 360$, while in the bottom row (d/e/f), $k/\delta = 1/6$.

difference between $\overline{u'\theta'}$ and $\overline{u'u'}$ indicates that the correlation between u' and θ' decreases as k^+ increases.

4. Effects of local roughness

While the previous section showed the effect of wall roughness on typical turbulence statistics, in this section we will focus more closely on near wall effects.

4.1. Structures and recirculation

In the roughness sub-layer, the flow is noticeably affected by local roughness features. Figure 10 shows that as k^+ is increased, the thermal streaks $\theta' < 0$ become much shorter and less coherent. Furthermore, for larger values of k^+, regions of $\theta' < 0$ do not necessarily coincide with regions where $u' < 0$ and high speed regions contain regions of both $\theta' < 0$ and $\theta' > 0$. This suggests that a velocity streak $u' < 0$ under the influence of wall roughness is less likely to consist of relatively cold fluid. As the similarity between the thermal and momentum streaks disappears for increasing k^+; the correlation between u'

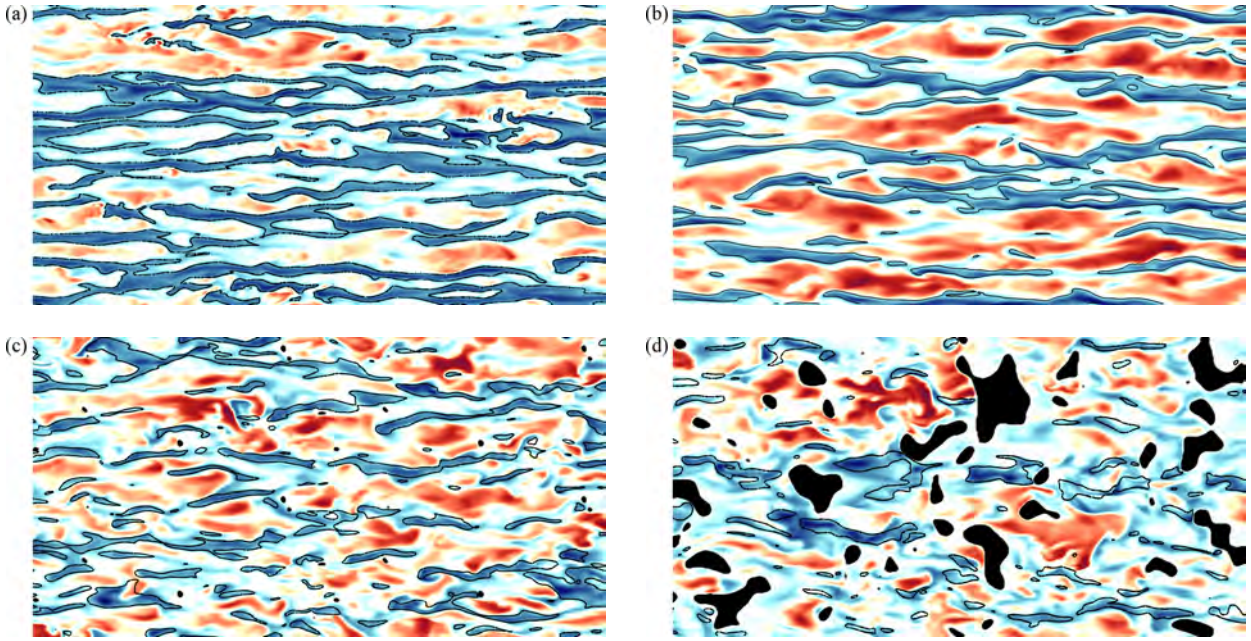

Figure 10: Temperature streaks at $y^+ = 15$, in the $Re_\tau = 360, k^+ = 0$ (a), $Re_\tau = 360, k^+ = 15$ (b), $Re_\tau = 360, k^+ = 30$ (c) and $Re_\tau = 360, k^+ = 60$ (d) cases. Blue regions correspond to $\theta' < 0$, while red regions correspond to $\theta' > 0$ regions. Black lines enclose regions where $u' < 0$. Solid black areas are surface protrusions.

and θ' decreases. A decreasing correlation between the velocity and temperature streaks is a physical explanation why the difference between the streamwise Reynolds stress and the streamwise Reynolds heat flux increases with wall roughness size.

The dissimilarity between the scalar and streamwise velocity fields is discussed further by investigating instantaneous fluctuations in the $y - z$-plane. It is well known that in smooth channel flows interfaces between neighbouring eddies are more visible in the scalar field than in the streamwise velocity field (see Antonia et al. [3], Pirozzoli et al. [33] and Abe and Antonia [1]). Despite the lower Reynolds numbers in the current study, similar observations can be made in figure 11. Particularly striking is the fact that close to the rough wall, the interfaces in the scalar field are much sharper than the interfaces in the velocity field. This indicates the scalar is less well mixed compared to the velocity close to the rough wall than further away. This is in line with the large effective Prandtl numbers (in the region $y/\delta < 0$) that we discussed in section 3.2. It was argued by Guezennec et al. [14] that the difference between scalar and velocity fields can be attributed to the role of the pressure; it is likely

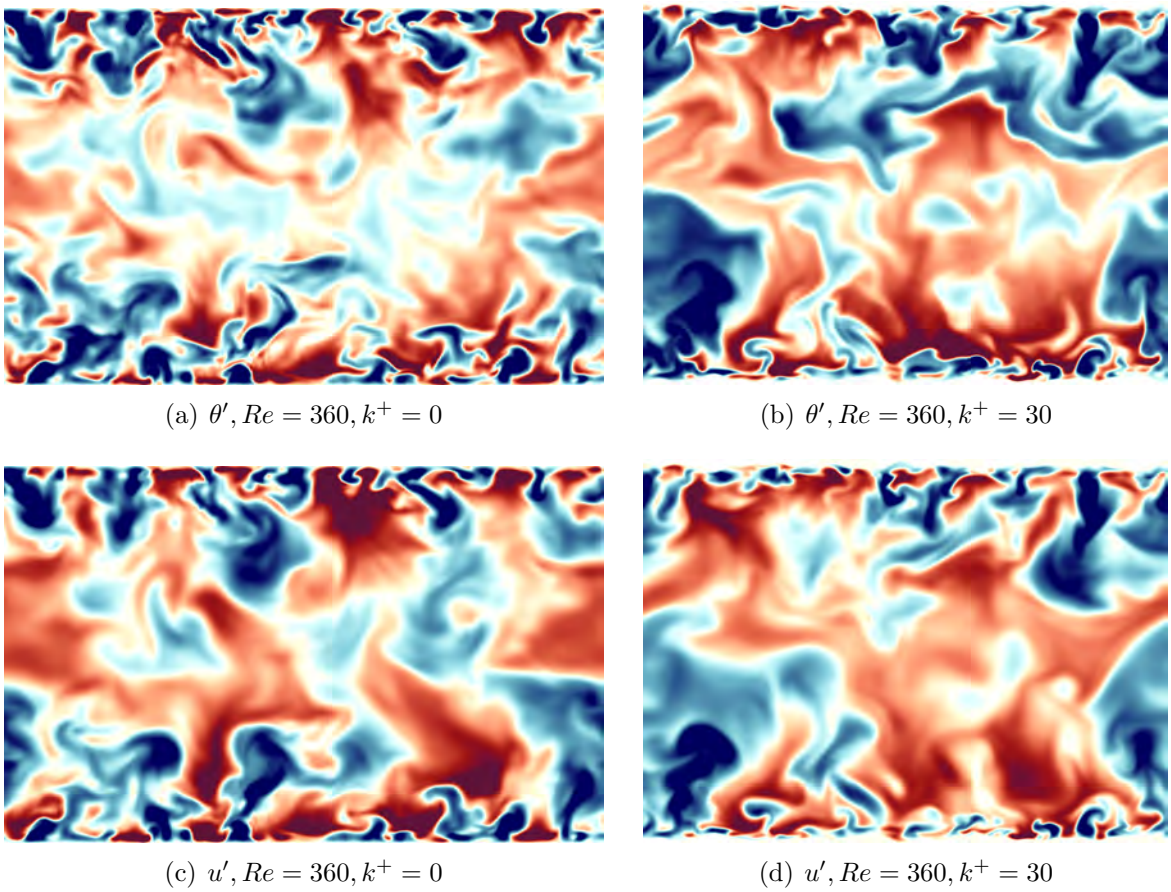

(a) $\theta', Re = 360, k^+ = 0$ (b) $\theta', Re = 360, k^+ = 30$

(c) $u', Re = 360, k^+ = 0$ (d) $u', Re = 360, k^+ = 30$

Figure 11: Instantaneous scalar and streamwise velocity fluctuation fields in the $y - z$-plane in a smooth channel and a channel with wall roughness.

that this role is enhanced in channels with rough walls.

Busse et al. [7] already showed that significant flow reversal zones exist in turbulent flows over the grit-blasted surface. Flow reversal zones typically exist near locations where $\partial s/\partial x < 0$. An instantaneous visualisation of a recirculation zone is shown in figure 12. The recirculation noticeably affects the near wall temperature field. Close to the windward slope ($\partial s/\partial x > 0$) relatively hot fluid (indicated by a light blue/white colour) is drawn in from the bulk, thereby creating a large temperature gradient at the surface. However, close to the downward slope, cold fluid (indicated by a dark blue colour) accumulates, which leads to a visibly smaller temperature gradient. The recirculation zones, formed as a result of adverse pressure gradients have a profound effect on the mean temperature and velocity

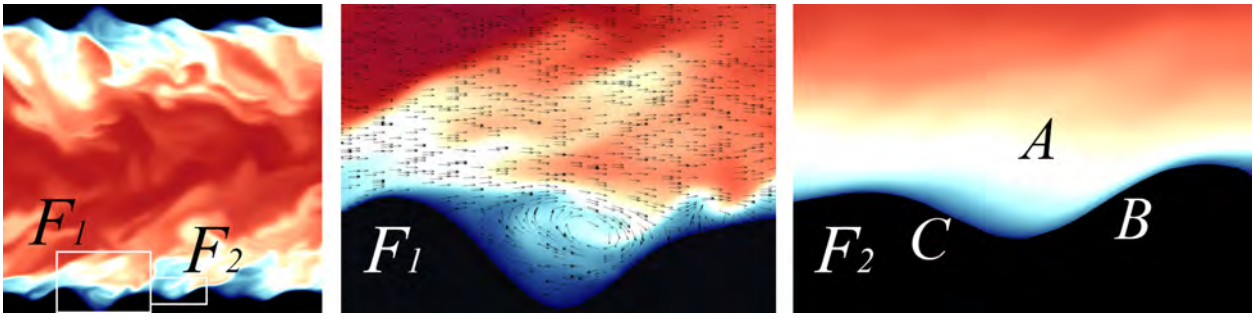

Figure 12: Left: part of the simulated channel with instantaneous temperature contours. Middle: instantaneous velocity vectors and close to a recirculation zone from frame F_1. Velocity vectors are not to scale. Right: time averaged temperature contours close to a recirucalation zone from frame F_2.

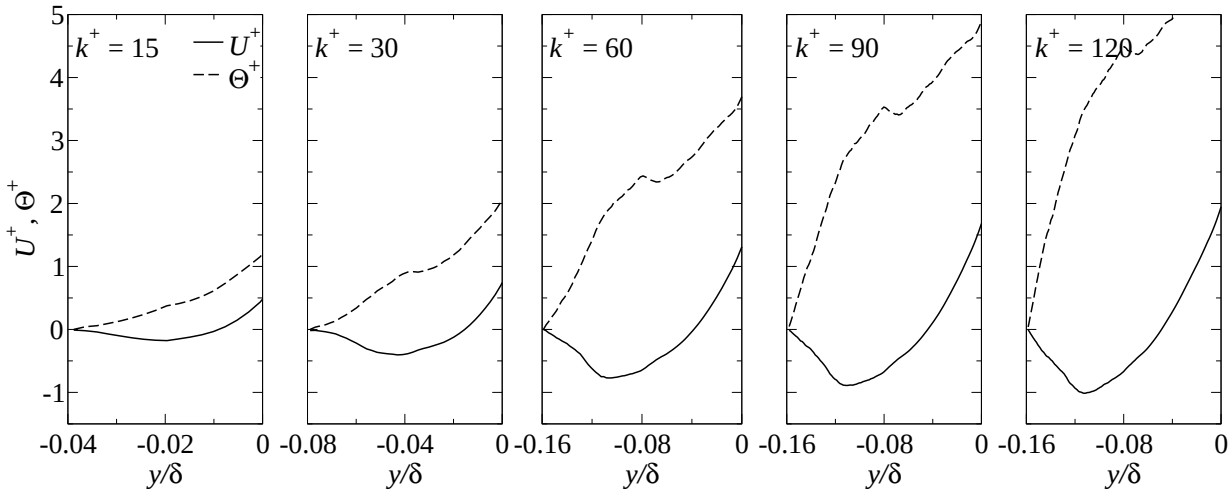

Figure 13: Velocity and temperature profiles well within the roughness sublayer.

field, as shown in figure 13. The strength of the recirculation is likely to increase as k^+ increases, which results in lower mean velocity values. As k^+ increases, hotter fluid can flow from the bulk region (figure 12, region A) into the roughness layer, which leads to higher mean temperatures inside the roughness layer (which is evident from figure 13). The relatively hot fluid then typically impinges on a windward slope (figure 12, region B). A thin thermal boundary layer is then formed that extends both in the streamwise direction (under the influence of mean streamwise momentum) as well as the opposite direction (under the influence of the recirculation zone and thus, an adverse pressure gradient), which ends as soon as it comes under the influence of mean streamwise momentum (figure 12, region C).

Figure 13 showcases the fact that, while an adverse pressure gradient affects momentum, there is no corresponding mechanism for heat transfer. The local maximum in the mean temperature profile that is seen in the k^+ =30, 60, 90 and 120 cases is the result of the irregular surface height in combination with the averaging procedure that was described in section 3.1.

4.2. Quadrant analysis

It has been shown that wall roughness has a profound effect on the velocity and thermal streaks close to the wall. It is well known that such regions give rise to the Reynolds shear stress $\overline{v'u'}$ and heat flux $\overline{v'\theta'}$, which in turn largely determine the skin friction factor and the Stanton number in smooth channels. Therefore, we will examine in more detail the structure of $\overline{v'u'}$ and $\overline{v'\theta'}$ using the quadrant analysis that was originally developed by Willmarth and Lu [38]. This method has proven to be a simple, but effective tool in the analysis of Reynolds shear stress, see Wallace [37]. The definition of the quadrants of the Reynolds shear stress is as follows: Q1: $u' > 0$ & $v' > 0$, Q2: $u' < 0$ & $v' > 0$, Q3: $u' < 0$ & $v' < 0$, Q4: $u' > 0$ & $v' < 0$. The definition of the heat flux quadrants is found by replacing u' with θ'., i.e. Q1: $\theta' > 0$ & $v' > 0$, Q2: $\theta' < 0$ & $v' > 0$, Q3: $\theta' < 0$ & $v' < 0$, Q4: $\theta' > 0$ & $v' < 0$. In a smooth channel with internal heating, Q2 and Q4 are the most frequent quadrants. These quadrants are known as ejections and sweeps (or outward motion of cold fluid and inward motion of hot fluid for heat transfer), respectively.

In figure 14, we compare the different quadrants of the Reynolds shear stress $u'v'$ with those of the turbulent heat flux $v'\theta'$. By comparing the quadrants for different wall roughness heights, it becomes clear that two distinct regions can be found, in which the quadrants show different behaviour. For different wall roughness heights, these regions show very similar behaviour. In the region $y^+ > k^+/3$, the probability distributions of events in each quadrant for both the heat flux and Reynolds shear stress are very similar to each other, which is also typical of the behaviour for a smooth channel, see also Perry and Hoffman [31]. For the Reynolds shear stress, the probability distribution of the different quadrants are equipartioned for $y^+ < -k^+/3$ and then rapidly diverge in the region $-k^+/3 < y^+ < k^+/3$.

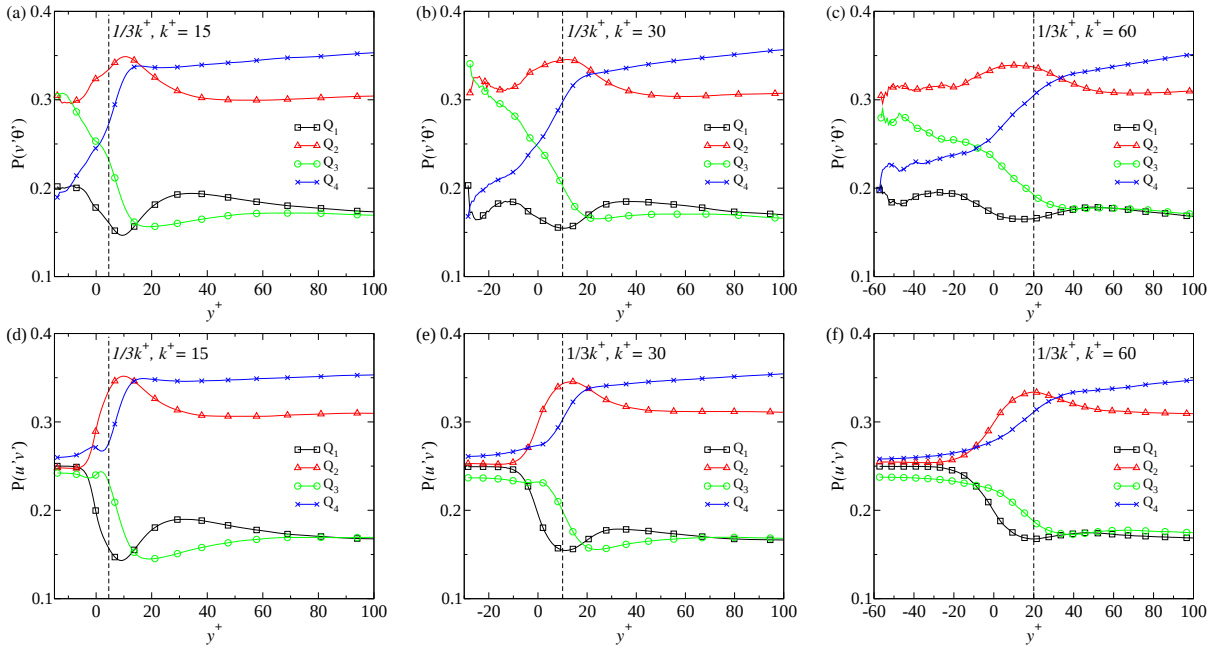

Figure 14: Quadrant probabilities of the Reynolds shear stress $v'u'$ and the turbulent heat flux $v'\theta'$ for $Re_\tau = 360$, $k^+ = 15$ (a/d) k^+=30 (b/e) and $k^+ = 60$ (c/f).

In the region $y^+ < k^+/3$, the heat flux quadrants show different behaviour compared to the Reynolds shear stress quadrants. In this region, the probability of Q3 events in $v'\theta'$ is enhanced, while the probability of Q4 in $v'\theta'$ events is diminished, when compared to the region $y^+ > k^+/3$. These results mean that the similarity in structure of the Reynolds stress and the heat flux breaks down for $y^+ < k^+/3$.

We continue the analysis of the Reynolds shear stress and heat flux quadrants by investigating the relative contributions $\langle\overline{v'u'}\rangle_j/\langle\overline{v'u'}\rangle$ and $\langle\overline{v'\theta'}\rangle_j/\langle\overline{v'\theta'}\rangle$, where j refers to the quadrant number, which are shown in figure 15. As before, the different contributions of the Reynolds shear stress quadrants are very similar to those of the heat flux in the region $y^+ > k^+/3$, which is again reminiscent of smooth channel behaviour (for a comparison with literature, see Abe and Antonia [1]). The relative contributions of the quadrants are different for $y^+ < k^+/3$. The absolute value of the Reynolds shear stress in each quadrant grows rapidly in this region. Since the total Reynolds shear stress changes sign twice in this region, discontinuous behaviour can be seen. In the same region, the heat flux quadrants behave differently. The most notable difference is that the relative magnitude of Q4 is larger than

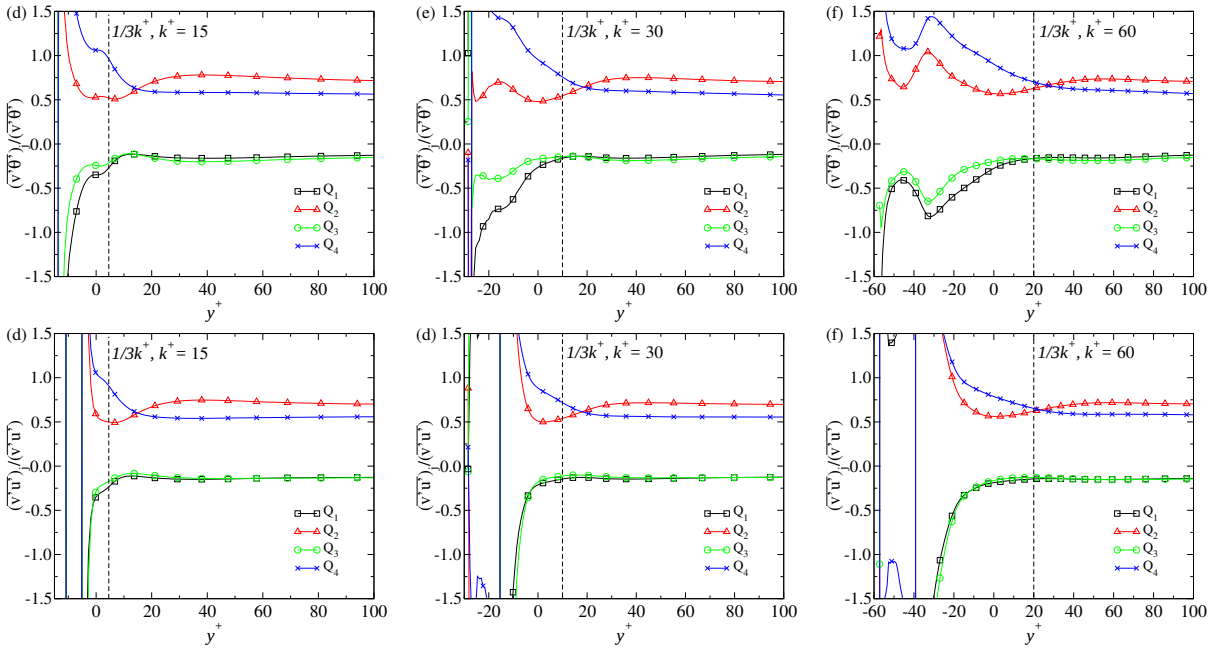

Figure 15: Quadrant analysis of the Reynolds shear stress $v'u'$ and the turbulent heat flux $v'\theta'$ for $Re_\tau = 360$, $k^+ = 15$ (a/d) k^+=30 (b/e) and $k^+ = 60$ (c/f).

Q2 for $y^+ < k^+3$, meaning that inward motions of relatively hot fluid are promoted.

4.3. Probability density functions

The structural changes seen in the previous section will be likely to affect the local heat transfer. An often-used non-dimensional measure of the local heat transfer coefficient is the Stanton number, $St \equiv q_w/(\rho U_b c_p(T_w - T_b))$. In smooth channels, this number is often related to the skin friction coefficient $C_f \equiv 2\tau/(\rho U_b^2)$ through the Reynolds analogy: $St = C_f/2$. However, since we investigate channels with rough walls, we will distinguish between the the local frictional drag T_x , which was shown by Peet and Sagaut [30] to be

$$T_x = -Re_\tau^{-1} \left(\boldsymbol{\nabla u} + (\boldsymbol{\nabla u})^T\right)\big|_s \, \hat{\boldsymbol{n}} \cdot \hat{\boldsymbol{x}} = -Re_\tau^{-1} \frac{\partial u}{\partial \hat{n}}, \tag{6}$$

and the local form drag F_x:

$$F_x = -p_s \hat{\boldsymbol{n}} \cdot \hat{\boldsymbol{x}} \tag{7}$$

In these equations, $\boldsymbol{x}$ is the unit streamwise vector, $\hat{\boldsymbol{n}}$ is the unit normal vector. The subscript s means that the quantity is evaluated at the surface. Similarly, q is the local heat

flux, defined as:

$$q_s = -Pe_\tau^{-1} \frac{\partial \theta}{\partial \hat{n}} \tag{8}$$

A local skin friction coefficient may be calculated as:

$$C_f^l \equiv \frac{2(T_x + F_x)}{\rho U_b^2}, \tag{9}$$

while a local Stanton number may be calculated as:

$$St^l \equiv \frac{q_s}{\rho c_p U_b T_b}, \tag{10}$$

Please note that T_x, F_x and q_s are instantaneous values.We compare probability density functions of both St^l and C_f^l for the $k^+ = 15, 30, 60$ cases at $Re_\tau = 360$ in figure 16. In the same figure, we also investigate the probabilities of St^l and C_f^l, conditioned on the presence of recirculation zones, $\mathrm{P}(St^l|\overline{u} < 0)$ or on the absence of recirculation $\mathrm{P}(St^l|\overline{u} > 0)$. All probability density functions in figure 16 have been scaled with the standard deviation of $\mathrm{P}(St^l)$ or $\mathrm{P}(C_f^l)$.

The general shape of $\mathrm{P}(St^l)$ and $\mathrm{P}(C_f)^l$ appears qualitatively similar, except for the fact that C_f^l can assume negative values. Inside the recirculation zones, the Stanton number is likely to be smaller than the global average; this corresponds well with Meinders et al. [25] observation that a recirculation zone acts as a thermal resistance. As k^+ increases, the area that is covered by a recirculation zone increases. The largest Stanton numbers are most likely to be found outside the recirculation zones. As k^+ increases, $\mathrm{P}(St^l|\overline{u} < 0)$ approaches $\mathrm{P}(St^l|\overline{u} > 0)$ for large values of the Stanton number. The effects of the recirculation zone on the Stanton number are similar for the friction coefficient; inside recirculation zones, C_f^l is likely to be smaller than zero and as k^+ increases, $\mathrm{P}(C_f^l|\overline{u} < 0)$ approaches $\mathrm{P}(C_f^l|\overline{u} > 0)$ for large friction coefficients. The fact that positive skin friction factors can be found inside the recirculation zone indicates that the zone can move in time.

4.4. Correlation between surface features and heat transfer

In flows with smooth walls, the near wall streaks are known to largely determine local skin friction and heat transfer. In section 4.1, local roughness protrusions were found

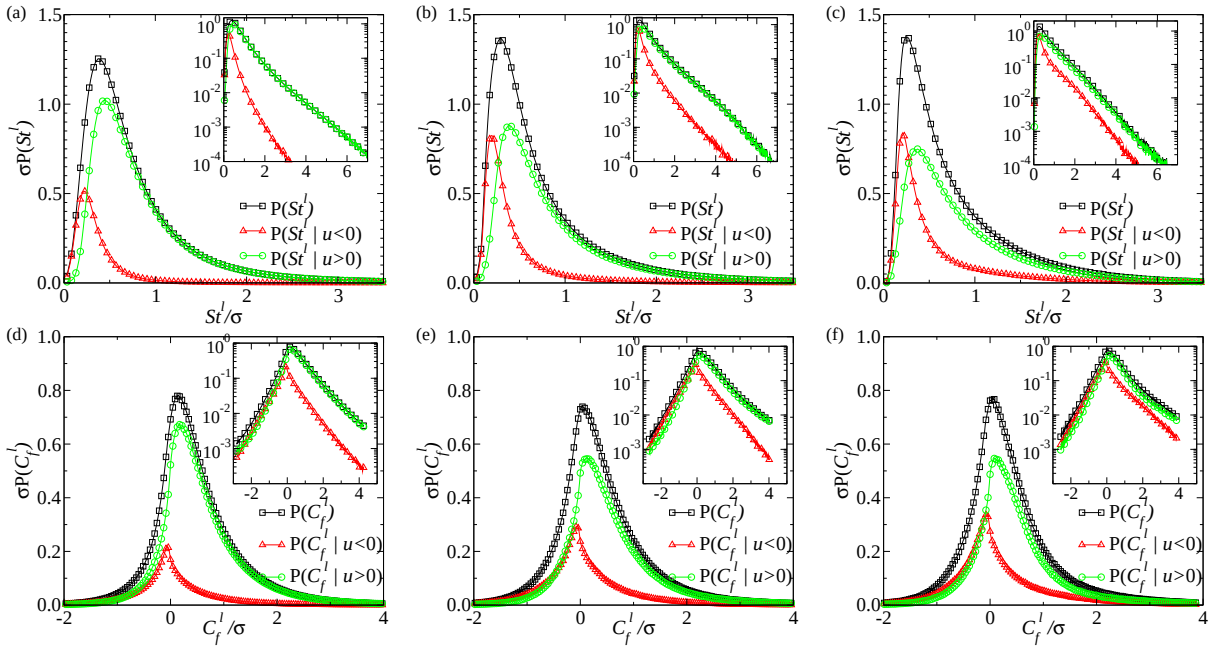

Figure 16: Probability density functions of the local Stanton numbers St^l (top row) and skin friction coefficients C_f^l (bottom row) for the cases $k^+ = 15$ (a/d), $k^+ = 30$ (b/e) and $k^+ = 60$ (c/f). $Re = 360$. σ denotes the standard deviation of $\mathrm{P}(St^l)$.

to break-up the streaks, which at least partially determine the local skin friction and heat transfer. Furthermore, it was shown in section 4.3 that inside recirculation zones, the Stanton number is likely to be much smaller than the average, which could be related to the accumulation of relatively cold fluid near downward slopes. Based on these observations, a

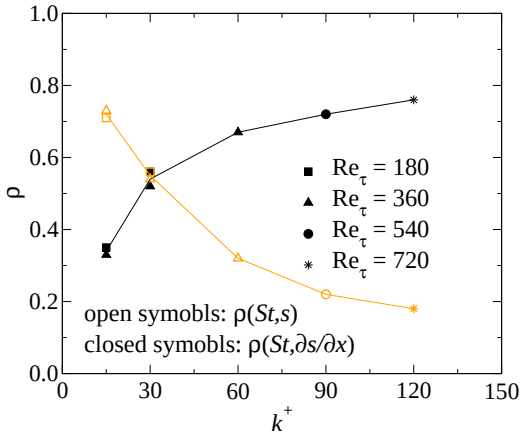

Figure 17: Correlation coefficients $\rho(s, St)$ and $\rho(\partial s/\partial x, St)$.

correlation between either the local surface height s or the local surface slope $\partial s/\partial x$ and the local Stanton number may exist. The correlation coefficents $\rho(s, St)$ and $\rho(\partial s/\partial x, St)$ are shown in figure 17. The correlation coefficient $\rho(s, St)$ decreases with increasing k^+, while $\rho(\partial s/\partial x, St)$ increases with k^+. This means that at small k^+, the influence of the local surface height is more important, which may be related to the break-up of the streaks. For fully rough conditions, the recirculation zones are much more important as local negative slopes typically yield low Stanton numbers, while windward slopes yield large Stanton numbers. This observation may be related to results that were presentated by Forooghi et al. [12]; with increasing mean slope, the heat transfer enhancement is less than the drag enhancement. This could be a result of the recirculation zones acting as a thermal resistance, while in the same region both friction and form drag contribute to the drag increase.

5. Parametrisation

In the previous sections, we have presented mean statistics and analysed the effect of local surface roughness on heat transfer. In this section, we will investigate whether these effects can be parametrised in relations that are simple to use.

5.1. Roughness function

Analogous to the momentum wall roughness function, $\Delta U^+(k_s^+)$, a function $\Delta\Theta^+ = \Theta^+|_{k_s^+=0} - \Theta^+|_{k_s^+}$ that parametrises the roughness effects on the temperature field in the log-region of the turbulent flow can be found. Figure 18(a) shows both the momentum and temperature wall roughness functions. It is clear that for all k^+, $\Delta U^+ > \Delta\Theta^+$. However, the DNS results for $\Delta\Theta^+(k_s^+, Pr)$ suggest a departure from smooth-wall conditions that is qualitatively similar to that of $\Delta U^+(k_s^+)$.

Kays and Crawford [18] describe a relation for a mean temperature profile with roughness as

$$\Theta^+ = \frac{Pr_t}{\kappa} \ln\left(\frac{32.6y^+}{k^+}\right) + \frac{5}{4}(k_s^+)^{0.2} Pr^{0.44} \tag{11}$$

The following relation for $\Delta\Theta^+(k_s^+, Pr)$ was derived by subtracting equation (11) from equa-

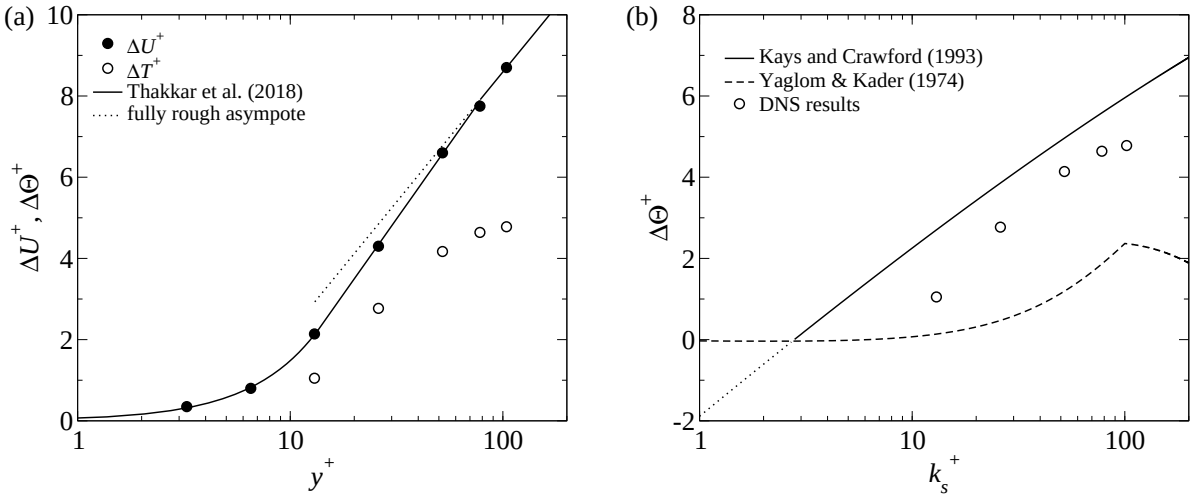

Figure 18: a) wall roughness function for momentum ΔU^+ and for temperature $\Delta\Theta^+$. b) the temperature roughness function (DNS results) along with estimates obtained from Kays and Crawford [18] and Yaglom and Kader [39].

tion (5):

$$\Delta\Theta^+ = \frac{Pr_t}{\kappa}\ln(k_s^+) + \beta'(Pr) - \frac{5}{4}(k_s^+)^{0.2}Pr^{0.44}, \tag{12}$$

where $\beta'(Pr) = \beta(Pr) - 7.4$. The form of equation (12) resembles the asymptotic behaviour of ΔU^+ that was found by Nikuradse [27] (i.e., $\Delta U^+(k_s^+) = 2.5\ln(k_s^+) - 2.98$ for $k_s^+ > 70$), with the exception of the last term on the right hand side.

Another estimate for $\Delta\Theta^+(k_s^+, Pr)$ can be obtained by considering a modification to $\beta(Pr)$ that was proposed by Yaglom and Kader [39] in order to account for wall roughness effects:

$$\beta_Y = \begin{cases} 0.01k_s^+\beta_r + (1 - 0.01k_s^+)\beta_s, & \text{if } k_s^+ < 100 \\ \beta_r, & \text{if } k_s^+ > 100, \end{cases} \tag{13}$$

where $\beta_r = 0.55\sqrt{k^+}(Pr^{2/3} - 0.2) - \frac{Pr_t}{\kappa}\ln(k^+) + 9.5$ and $\beta_s \equiv 12.5Pr^{2/3} - 6$. Please note that the value of $\beta_s \approx \beta$. This results in the following temperature wall roughness function:

$$\Delta\Theta^+ = \begin{cases} 0.01k_s^+(\beta - \beta_r), & \text{if } k_s^+ < 100 \\ \beta - \beta_r, & \text{if } k_s^+ > 100. \end{cases} \tag{14}$$

For $k_s^+ > 100$, equation (14) yields:

$$\Delta\Theta^+ = \frac{Pr_t}{\kappa}\ln(k^+) + \beta''(Pr) - 0.55\sqrt{k^+}(Pr^{2/3} - 0.2), \tag{15}$$

where $\beta''(Pr) = \beta(Pr) - 9.5$. The form of equation (15) is very similar to that of (12). However, equation (15) yields decreasing values of $\Delta\Theta$ for increasing values of k^+ for $k_s^+ > 100$, which equation (12) does not.

Equations (12) and (14) are shown together with the DNS results in figure 18(b). The DNS results lie between both estimates. The discrepancy between the DNS results and equation (4) results partially from the fact that a fully rough regime is assumed by Kays and Crawford [18]. Moreover, the equation by Kays and Crawford [18] depends on the results that were obtained by Dipprey and Sabersky [9], who used a different kind of wall roughness. Furthermore, the factor $\frac{5}{4}$ was determined by Pimenta et al. [32] from data that were obtained from a rough surface consisting of closely packed spheres.

5.2. Stanton number relations

The estimation of $\Delta\Theta^+(k_s^+, Pr)$ is important as it contributes linearly to the integrated mean scalar Θ_b^+ as,

$$\Theta_b^+ = \frac{Pr_t}{\kappa}\left(\ln(Re_\tau) - 1\right) + \beta(Pr) - \Delta\Theta(k_s^+, Pr), \tag{16}$$

which in turn is closely related to the Stanton number (for a volumetrically heated channel),

$$St = \frac{\sqrt{C_f/2}}{\Theta_b^+}, \tag{17}$$

see Abe and Antonia [1]. Similar equations can be found for the bulk velocity and the skin friction factor:

$$U_b^+ = \frac{1}{\kappa}\left(\ln(Re_\tau) - 1\right) + 5.1 - \Delta U^+(k_s^+), \tag{18}$$

and

$$C_f = \frac{2.0}{(U_b^+)^2}. \tag{19}$$

Since we have defined u_τ as $\sqrt{-(\delta/\rho)\Pi}$, C_f measures both frictional and form drag. In smooth channels, equation (16) yields errors of less than 1% when compared to the relation

Table 3: Stanton number – friction factor analogy errors. The error is calculated as $(St_{DNS} - St_R)/(St_{DNS})$, where St_{DNS} is the Stanton number that is directly calculated from the DNS results, while St_R is the Stanton number that is calculated using the relations indicated in the table. In the first column, $\Delta\Theta^+$ stems from the DNS results. In the second and third column, $\Delta\Theta^+$ was taken from listed equations. Errors are listed in percentages.

	$\Delta\Theta^+$ DNS & Eqn. (17)	$\Delta\Theta^+$ Eqn. (12)& Eqn. (17)	$\Delta\Theta^+$ Eqn. (14)& Eqn. (17)
$k^+ = 15$	0.4	10.5	-5.00
$k^+ = 30$	1.0	7.61	-13.3
$k^+ = 60$	1.3	7.70	-16.8
$k^+ = 90$	2.2	8.30	-15.7
$k^+ = 120$	2.7	11.1	-12.9

given by Abe and Antonia [1], i.e. $\Theta_b^+ = 2.18\ln(Re_\tau)+1.3$, for the range $Re_\tau = 200-10000$, when $Pr = 0.71$ and $Pr_t = 0.85$. The results in table 3 show that the assumption of a log-law for the complete temperature profile (not including the near-wall and wake regions) does not lead to large errors. In other words, equations (16) & (17) yield very good estimations of the heat transfer coefficient, as long as the temperature wall roughness function is known. Therefore, equation (12) yields better results than (14).

Different St-friction factor analogies have been presented in the past, such as:

$$\left(\frac{2St}{C_f}\right)^{-1} = 5\sqrt{C_f/2}\left[Pr + \ln(1+5Pr) + \frac{1}{2}\ln\left((Re/60)\sqrt{C_f/2}\right)\right] \tag{20}$$

by Martinelli [24],

$$St = \frac{C_f/2}{1 + 1.5Re^{-1/8}Pr^{-1/6}[PrC_f/C_{f,s} - 1]} \tag{21}$$

by Nunner [28], and

$$St = \frac{C_f/2}{1 + \sqrt{C_f/2}\{k_f[Re\sqrt{C_f/2}(\epsilon_s/D)]^{0.2}Pr^{0.44} - 8.48\}} \tag{22}$$

by Dipprey and Sabersky [9]. These relations are compared with the DNS results in table 4. The Reynolds analogy yields an increasing error for larger k^+; this result is in line with Bons [5] and Forooghi et al. [13]. The increase in error can be directly related to the difference in the bulk temperature and the bulk velocity (equations (16) and (18)), which in turn stems from the difference between $\Delta\Theta^+$ and ΔU^+ that was shown in figure 18(left).

Table 4: Stanton number – friction factor analogy errors. Errors are calculated as is indicated in the caption of table 3.

	Reynolds analogy	Dipprey/Sabersky analogy	Martinelli analogy
$k^+ = 0$	-2.35	-13.2	30.8
$k^+ = 15$	3.17	-12.9	19.5
$k^+ = 30$	7.54	-0.07	4.01
$k^+ = 60$	16.2	-0.02	-7.43
$k^+ = 90$	23.1	-0.05	-6.10
$k^+ = 120$	30.0	-0.10	-2.45

Table 5: Stanton number predictions based on the Reynolds analogy factor. Errors are calculated as is indicated in the caption of table 3. *For equation (12), $k^+ = 0.001$ was used, instead of $k^+ = 0.0$

	Aupoix relation + DNS	Aupoix relation + eq. (12)	Forooghi relation
$k^+ = 0$	0.00	-48.3*	2.35
$k^+ = 15$	-1.40	8.41	1.26
$k^+ = 30$	-0.82	5.55	1.26
$k^+ = 60$	-0.64	5.57	1.11
$k^+ = 90$	1.22	7.16	1.96
$k^+ = 120$	1.36	6.85	2.29

The Martinelli equation shows an opposite trend; as k^+ increases, the difference between the DNS results and the Martinelli equation decreases. Finally, the equation by Dipprey & Sabersky yields reasonable results in the range $k^+ = 30 - 120$, but yields an unsatisfactory result at $k^+ = 0$.

More recently, researchers have sought after a relation between the Reynolds analogy factor $RA \equiv 2St/C_f$ and the wall roughness parameter k. Aupoix [4] derived the following relation:

$$\frac{RA}{RA_0} = \frac{1 - \Delta U^+ \sqrt{C_{f,0}}}{1 - RA_0 \Delta\Theta^+ \sqrt{C_{f,0}}}, \tag{23}$$

in which the subscript '0' refers smooth wall conditions. Forooghi et al. [12] proposed the following relation:

$$\frac{RA}{RA_0} = 0.55 + 0.45 \exp\left\{-k_s^+/130\right\}. \tag{24}$$

Predictions by equation 23 and 24 are compared with the DNS results in table 5. Equation (23) in combination with the DNS results yields excellent results. However, combining equation (23) with (12) yields large errors for small k^+. This result shows that accurate knowledge of $\Delta\Theta^+$ is necessary for credible heat transfer predictions in flows over rough walls. On the other hand, the DNS results are in very good agreement with equation (24).

6. Conclusions and discussion

We have analysed the effect of wall roughness on turbulent heat transfer. Wall roughness affects heat transfer and momentum transfer differently. The temperature and momentum wall roughness functions differ significantly: $\Delta\Theta^+$ is substantially smaller than ΔU^+ at $Pr = 1$. This difference stems from the fact that high temperature fluid from the bulk region penetrates into the roughness layer. This results in the wall-scaled mean temperature profile being much larger than the mean velocity profile (which is largely negative due to the effect of pressure) inside the roughness layer. This translates into temperature values being larger than mean velocity values in the bulk region as well. The difference between $\Delta\Theta^+$ and ΔU^+ accounts directly for the failure of the Reynolds analogy for fully rough conditions. This is in-line with literature since the result that $\Delta U^+ > \Delta\Theta^+$ can be traced to the fact that the velocity field is affected by pressure, while there is no corresponding mechanism for the thermal field.

Wall roughness also affects the near wall cycle. The velocity and temperature streaks are broken up by local wall roughness protrusions. This effect causes the time- and spatially-averaged temperature fluctuations to decrease for increasing wall roughness size. While the wall normal Reynolds stress $\overline{v'u'}$ and heat flux $\overline{v'\theta'}$ decrease for larger wall roughness size, their respective magnitudes remain very similar for different k^+. In contrast, the structure of the wall normal Reynolds shear stress and the heat flux is affected. In the roughness layer, for $y^+ < k^+/3$, quadrants of the Reynolds shear stress are affected differently than the quadrants of the heat flux. However, it should be noted that the magnitude of the heat flux $u'\theta'$ is very small here. Therefore, it can be argued that the wall roughness effect on the quadrants of $v'u'$ and $v'\theta'$ contribute to the failure of the Reynolds analogy only in a minor

fashion.

The similarity and therefore correlation between the velocity and the temperature streaks decreases for increasing wall roughness, which results in a decrease in the magnitude of the streamwise heat flux $u'\theta'$. In smooth channels, only the wall normal heat flux $v'\theta'$ contributes to the mean Stanton number. However, it is conceivable that the streamwise heat flux contributes to local Stanton numbers in parts of the channel where the surface slope is steep. Furthermore, the difference between $u'u'$ and $u'\theta'$ increases for larger k^+. Thus, it is also conceivable that the difference between $u'u'$ and $u'\theta'$ for increasing k^+ contributes to the failure of the Reynolds analogy, as $u'u'$ and $u'\theta'$ contribute differently to C_f and St, respectively.

By studying probability density functions of the instantaneous Stanton number, the recirculation zones were found to have a detrimental effect on heat transfer. This observation, and that of the break-up of streaks has led to the conclusions that 1) for small k^+, the instantaneous Stanton number and the local height of the rough surface are well correlated and that 2) for $k^+ > 60$, the slope and the instantaneous local Stanton number are correlated.

Finally, it should be noted that the results in this paper were obtained on a single rough surface. It is well known that different rough surfaces yield different results for ΔU^+ and the same could be true for $\Delta\Theta^+$. It is also unknown how the thermal field will be affected by wall roughness at Prandtl numbers not equal to unity. The relations for Θ^+ that were derived from empirical relations found in the literature do depend on the Prandtl number and may serve as a guideline for a general relation for $\Delta\Theta^+$ in the future.

Acknowledgments

This work is part of a computing research programme with project number 16661, which is (partly) financed by the Netherlands Organisation for Scientific Research (NWO). This work was carried out on the Dutch national e-infrastructure with the support of SURF Cooperative.

References

[1] H. Abe and R. A. Antonia. Relationship between the heat transfer law and the scalar dissipation function in a turbulent channel flow. *Journal of Fluid Mechanics*, 830:300–325, 2017.

[2] H. Abe and R. A. Antonia. Mean temperature calculations in a turbulent channel flow for air and mercury. *International Journal of Heat and Mass Transfer*, pages 1152–1165, 2019.

[3] R. A. Antonia, H. Abe, and H. Kawamura. Analogy between velocity and scalar fields in a turbulent channel flow. *Journal of fluid mechanics*, 628:241–268, 2009.

[4] B. Aupoix. Improved heat transfer predictions on rough surfaces. *International Journal of Heat and Mass Transfer*, 56:160–171, 2015.

[5] J. Bons. A critical assessment of Reynolds analogy for turbine flows. *Transactions of the ASME*, 127:472–485, 2005.

[6] A. Busse, M. Lützner, and N. D. Sandham. Direct numerical simulation of turbulent flow over a rough surface based on a surface scan. *Computers & Fluids*, 116:129–147, 2015.

[7] A. Busse, M. Thakkar, and N. D. Sandham. Reynolds-number dependence of the near-wall flow over irregular rough surfaces. *Journal of Fluid Mechanics*, 810:196–224, 2017.

[8] O. Coceal, T.G. Thomas, I.P. Castro, and S.E. Belcher. Mean flow and turbulence statistics over groups of urban-like cubical obstacles. *Boundary-Layer Meteorology*, 121: 491–519, 2006.

[9] D. F. Dipprey and R. H. Sabersky. Heat and momentum transfer in smooth and rough tubes at various Prandtl numbers. *International Journal of Heat and Mass Transfer*, 6: 329–353, 1963.

[10] E. A. Fadlun, R. Verzicco, P. Orlandi, and J. Mohd-Yusof. Combined immersed-boundary finite-difference methods for three-dimensional complex flow simulations. *Journal of Computational Physics*, 24:35–60, 2000.

[11] K. A. Flack. Moving beyond Moody. *Journal of Fluid Mechanics*, 842:1–4, 2018.

[12] P. Forooghi, M. Stripf, and B. Frohnapfel. A systematic study of turbulent heat transfer over rough walls. *International Journal of Heat and Mass Transfer*, 127:1157–1168, 2018.

[13] P. Forooghi, A. Weidenlener, F. Magagnato, B. Böhm, H. Kubach, T. Koch, and B. Frohnapfel. DNS of momentum and heat transfer over rough surfaces based on realistic combustion chamber deposits. *International Journal of Heat and Fluid Flow*, 69:83–94, 2018.

[14] Y. Guezennec, D. Stretch, and J. Kim. The structure of turbulent channel flow with passive scalar transport. *Proceedings of the Summer Pogram. Center for Turbulence Research, Stanford University*, pages 127–138, 1990.

[15] B. A. Kader. Temperature and concentration profiles in fully turbulent boundary layers. *International Journal of Heat and Mass Transfer*, 24(9):1541–1544, 1981.

[16] B. A. Kader and A. M. Yaglom. Heat and mass transfer laws for fully turbulent wall flows. *International Journal of Heat and Mass Transfer*, 15:2329–2351, 1972.

[17] K. Katoh, K.-So Choi, and T. Azuma. Heat-transfer enhancement and pressure loss by surface roughness in turbulent channel flows. *International Journal of Heat and Mass Transfer*, 43:4009–4017, 2000.

[18] W. M. Kays and M. E. Crawford. *Convective heat and mass transfer*. McGraw-Hill, New York, 1993.

[19] J. Kim and P. Moin. Transport of passive scalars in turbulent channel flow. *NASA Technical Memorandum 89463*, 1987.

[20] J. Kim, P. Moin, and R. Moser. Turbulence statistics in fully developed channel flow at low Reynolds number. *Journal of Fluid Mechanics*, 177:138–166, 1987.

[21] H. Kong, H. Choi, and J. S. Lee. Dissimilarity between the velocity and temperature fields in a pertubed turbulent thermal boundary layer. *Physics of Fluids*, 13:1466–1479, 2001.

[22] L. D. Landau and E. M. Lifshitz. *Fluid Mechanics (2^{nd} edition)*. Pergamon Press, 1987. 1^{st} edition appeared in 1949.

[23] S. Leonardi, P. Orlandi, L. Djenidi, and R. A. Antonia. Heat transfer in a turbulent channel flow with square bars or circular rods on one wall. *Journal of fluid mechanics*, 776:512–530, 2015.

[24] R. C. Martinelli. Heat transfer to molten metals. *Trans. ASME*, 69:947, 1947.

[25] E. R. Meinders, K. Hanjalic, and R. J. Martinuzzi. Experimental study of the local convection heat transfer from a wall-mounted cube in turbulent channel flow. *ASME Journal of heat transfer*, 121:564–573, 1999.

[26] Y. Nagano, H. Hattori, and Tomoya Houra. DNS of velocity and thermal fields in turbulent channel flow with transverse-rib roughness. *International Journal of Heat and Fluid Flow*, 25:393–403, 2004.

[27] J. Nikuradse. Strömungsgesetze in rauhen Rohren. *Beilage zu Forschung auf dem Gebiet des Ingenieurwesens*, Forschungsheft 361, Ausgabe B Band 4, 1933.

[28] W. Nunner. Heat transfer and pressure drop in rough tubes. *VDI-Forshungsheft 455, Series B*, 22:5–39, 1956.

[29] P. Orlandi, D. Sassun, and S. Leonardi. DNS of conjugate heat transfer in presence of rough surfaces. *International Journal of Heat and Mass Transfer*, 100:250–266, 2016.

[30] Y. Peet and P. Sagaut. Theoretical prediction of turbulent skin friction on geometrically complex surfaces. *Physics of fluids*, 21:105105, 2009.

[31] A. E. Perry and P. H. Hoffman. An experimental study of turbulent convective heat transfer form a plate. *Journal of Fluid Mechanics*, 77:355–368, 1976.

[32] M. M. Pimenta, R. J. Moffat, and W. M. Kays. *Report HMT-21.* Thermosciences Division, Department of Mechanical Engineering, Stanford University, 1975.

[33] S. Pirozzoli, M. Bernardini, and P. Orlandi. Passive scalars in turbulent channel flow at high Reynolds number. *Journal of fluid mechanics*, 788:614–639, 2016.

[34] P.R. Spalart and M. Kh. Strelets. Mechanisms of transition and heat transfer in a separation bubble. *Journal of Fluid Mechanics*, 403:329–349, 2000.

[35] M. Thakkar, A. Busse, and N. D. Sandham. Surface correlations of hydrodynamically drag for transitionally rough engineering surfaces. *Journal of Turbulence*, 18:138–169, 2016.

[36] M. Thakkar, A. Busse, and N. D. Sandham. Direct numerical simulation of turbulent channel flow over a surrogate for Nikuradse-type roughness. *Journal of Fluid Mechanics*, 837:R1–11, 2018.

[37] J. M. Wallace. Quadrant analysis in turbulence research: History and evolution. *Annual Review of Fluid Mechanics*, 48:131–158, 2016.

[38] W. W. Willmarth and S. S. Lu. Structure of the Reynolds stress near the wall. *Journal of Fluid Mechanics*, 55:65–92, 1972.

[39] A. M. Yaglom and B. A. Kader. Heat and mass transfer between a rough wall and turbulent fluid flow at high Reynolds and Peclét numbers. *Journal of Fluid Mechanics*, 62(3):601–623, 1974.